Electrochemistry Communications 192–193 (2026) 108243

Contents lists available at ScienceDirect

Electrochemistry Communications

journal homepage: www.elsevier.com/locate/elecom

Short communication

Decoupling mass-transport contributions in vanadium flow battery using electrochemical impedance spectroscopy

Zuzanna Borowiak [a,b], Jie Sun [a], Adam H. Whitehead [a], Frank Rhein [b,*]

[a] CellCube Energy Storage GmbH, IZ NÖ-Süd Strasse 3, Objekt M36, Wiener Neudorf, 2355, Austria
[b] Karlsruhe Institute of Technology, Institute of Mechanical Process Engineering and Mechanics, Strasse am Forum 8, Karlsruhe, 76131, Germany

ARTICLE INFO

Keywords:
EIS
VFB
Mass-transport
Low-frequency
Diffusion
Convection

ABSTRACT

The low-frequency mass-transport region of flow battery (FB) impedance spectra is commonly attributed to finite-diffusion processes, however, previous studies have not clearly distinguished between diffusion- and convection-dominated features. Here, two VFB cells with identical geometric electrode area but different flow orientations are studied by electrochemical impedance spectroscopy, exploiting a fourfold difference in cross-sectional area perpendicular to flow direction to differentiate the impact of those two effects. Comparison of the two orientations reveals that the low-frequency region contains two distinct contributions that respond differently to volumetric flow rate and mean linear velocity and are therefore consistent with different physical processes. These findings allow identification of the diffusion-dominated and convection-dominated contributions, which are essential for flow cell modelling and optimisation.

1. Introduction

Flow batteries (FBs) and particularly vanadium flow batteries (VFBs) have emerged as one of the most technically mature electrochemical energy storage for grid scale stationary applications, owing to their independently scalable power and energy capacities together with long cycle life [1]. Electrochemical reactions occur at porous carbon felt electrodes, where the V^{2+}/V^{3+} and VO^{2+}/VO_2^+ redox couples operate at the negative and positive electrodes, respectively. It is not trivial to model felt electrodes, due to their three dimensional structure with distinct ionically and electronically conducting pathways [2]. Performance is ultimately constrained by ohmic, kinetic, and mass-transport losses at these felts, and resolving how each contribution responds to operating conditions remains a challenge for both cell optimisation and modelling.

Electrochemical impedance spectroscopy (EIS) has become the primary tool for separating those contributions in FBs. However, due to the complex structure of porous felts, impedance features are challenging to interpret in terms of individual physical processes, and any interpretation must account for the distributed character of the electrode response [3]. While ohmic and kinetic contributions have been relatively well established in the literature, mass-transport has emerged as a particularly challenging phenomenon, as it involves the hydrodynamics of electrolyte flow through the pore network and diffusion at the fibre surface simultaneously [4–7]. Even in batteries without circulating electrolyte, Qu et al. cautioned that Warburg-type diffusion elements are not physically appropriate for describing transport in distributed porous electrodes, where pore accessibility and electrochemical utilisation are frequency dependent [8].

Sun et al. and Pezeshki et al. referred to the mass-transport region in VFB spectra as a finite-diffusion contribution and demonstrated that it is strongly flow rate dependent [4,5]. They described it as a complex phenomenon governed by the Nernstian diffusion layer and bulk electrolyte concentration, strongly influenced by felt morphology and the local velocity field. In equivalent circuit interpretation, Sun et al. represented this contribution as a resistor and constant phase element in series, explicitly acknowledging that the coupled diffusion–convection relationship cannot be adequately captured by a Warburg element alone [6]. Zhang et al. went further and divided the mass-transport region into two separate contributions, fitting separate equivalent circuit elements to each [7].

This interpretation is consistent with distribution of relaxation times (DRT) analysis, which deconvolutes impedance spectra without imposing an equivalent circuit model. DRT has revealed that the low-frequency mass-transport region contains multiple overlapping processes rather than a single one, as demonstrated by Schneider et al. and Schilling et al. [9–11]. The implication is significant: what is treated as a single mass-transport phenomena in VFB impedance spectra likely reflects at least two physical processes, which may be governed by different mechanisms and therefore respond differently to changes in flow conditions.

* Corresponding author.
E-mail address: frank.rhein@kit.edu (F. Rhein).

https://doi.org/10.1016/j.elecom.2026.108243
Received 6 July 2026; Received in revised form 13 August 2026; Accepted 16 August 2026
Available online 22 August 2026

This raises a problem that the existing literature has not yet fully addressed. Most experimental EIS studies in FBs vary flow conditions simply by changing the volumetric flow rate at fixed cell geometry, leaving volumetric flow rate and mean linear electrolyte velocity coupled throughout. Some studies have accounted for differences in mean linear velocity when comparing electrodes of different thicknesses or compression ratios, recognising that the same volumetric flow rate produces different local velocities as the cross-sectional area perpendicular to flow changes [12,13]. However, in these cases the velocity correction arises as a consequence of geometric and morphological differences between electrodes rather than as a deliberate experimental variable. To the best of our knowledge, no study has systematically varied both volumetric flow rate and mean linear velocity independently while keeping the geometric electrode area fixed. This means it has not been established whether a flow dependent impedance feature is driven by the total electrolyte supply to the cell or by the local velocity at the fibre surface - a distinction that directly determines which physical mechanism governs that feature and how it should be modelled.

In this work, VFB cells containing carbon felt electrodes of identical geometric area but different flow orientations are studied by EIS. Changing the electrode orientation varies the cross-sectional area perpendicular to the flow direction, allowing volumetric flow rate and mean linear velocity to be varied independently. By examining how individual features in the low-frequency transport region of the impedance spectra respond to each variable, this study aims to assign physical meaning to distinct mass-transport contributions and determine whether they are governed primarily by total electrolyte supply or by local electrolyte velocity.

2. Methods

2.1. Experimental setup

The experimental setup consisted of three VFB cells with anion exchange membranes connected to a shared electrolyte circuit made of two tanks (posolyte and negolyte) as shown in Fig. 1a. A main cell with electrode dimensions of 4 cm × 5 cm was used to adjust the electrolyte state-of-charge (SOC). Two smaller cells, hereafter referred to as *landscape* and *portrait*, were hydraulically connected to the same electrolyte loop but remained electrically isolated from the main cell throughout all measurements. Each measurement cell was connected individually to the potentiostat in turn. Both *landscape* and *portrait* contained graphitised carbon felt electrodes in a flow-through configuration with identical geometric area of 4 cm^2, but they differed in their electrode orientation relative to the flow direction. In the *landscape* cell the electrolyte flow entered along the shorter, W_1 edge, and in the *portrait* orientation, the flow entered along the longer, W_2 edge. Both felt electrodes of 96% porosity were compressed to the same thickness, T. This difference in orientation changes the cross-sectional area perpendicular to the flow direction, and therefore the mean linear electrolyte velocity at a given volumetric flow rate according to Eq. (1):

$$u = \frac{Q}{\epsilon A_{\perp}} \tag{1}$$

where u is the mean linear flow velocity, Q is the volumetric flow rate, ϵ is the porosity of the felt and $A_{\perp}$ is the cross-sectional area perpendicular to the flow direction. The resulting geometric properties of each configuration are summarised in Table 1 and visualised in Fig. 1b.

2.2. Measurements

Starting from V(III)/V(IV) electrolyte mixture, the target SOC was established using the main cell. The electrolyte flow was then diverted sequentially to *landscape* and *portrait*, and EIS spectra were recorded at volumetric flow rates of 5 ± 1 and 20 ± 1 mL min^{-1} and at 10% and 65% SOC (which corresponds to 1.27 ± 0.01 and 1.44 ± 0.01 V, respectively) for each cell. Performing measurements on both cells within the same electrolyte circuit and charging sequence aimed to maximise chance of *landscape* and *portrait* characterisation under comparable electrolyte composition and temperature.

Table 1
Geometric dimensions and calculated cross-sectional area perpendicular to the flow direction for felt electrodes in *landscape* and *portrait* orientations, where uncertainty in felt thickness was estimated based on variations arising from electrode compression and assembly tolerances.

Cell	L [cm]	W [cm]	T [cm]	$A_{\perp}$ [cm^2]
Landscape	1	4	0.35 ± 0.02	1.40 ± 0.08
Portrait	4	1	0.35 ± 0.02	0.35 ± 0.02

EIS measurements were performed using a Gamry Reference 3000 potentiostat (Gamry Instruments, USA) in galvanostatic mode at ambient temperature of 297 K with an applied sinusoidal AC perturbation current of 20 mA RMS. EIS spectra were recorded at 10 points per decade from 200 kHz to a lower limit of 25, 12, 10 mHz for 10% SOC *landscape* 20 mL min^{-1}, *landscape* 5 mL min^{-1}, *portrait* 5 mL min^{-1}, respectively and 31, 15, 12 mHz for 65% SOC *landscape* 20 mL min^{-1}, *landscape* 5 mL min^{-1} and *portrait* 5 mL min^{-1}, respectively. The lower frequency limit varies, as the measurements were terminated once the low-frequency arc had visually closed. Acquisition of each EIS spectrum required approximately 20 min.

2.3. Data extraction

EIS spectra were processed using the Python package *impedance.py* [14]. All spectra were validated using the linear Kramers–Kronig (Lin-KK) consistency test, with all residuals below 1% across the measured frequency range. Representative residuals are shown in Fig. 2 [15]. The empirical equivalent-circuit model shown in Fig. 3a was used to extract the two low-frequency contributions. The characteristic frequencies of features ***C*** and ***D*** were constrained to below 0.15 Hz and 0.15–30 Hz, respectively. The fitted characteristic frequencies remained well within these limits. The circuit was used only for parameter extraction; the physical assignments were based on the responses to volumetric flow rate and mean linear velocity, rather than on the equivalent-circuit structure or imposed frequency constraints. All fitted parameters and their standard errors are reported in Table 3.

3. Results and discussion

EIS measurements were performed at 10% SOC, where the small ***D*** feature becomes pronounced enough to measure accurately, and at 65% SOC to examine the SOC dependence [16]. Representative spectra for the *landscape* cell are shown in Fig. 3b, exhibiting the features typical of VFB impedance spectra: a high-frequency series ohmic resistance, followed by a response arising from distributed ionic and electronic conduction through the porous felt, a mid-frequency charge-transfer semicircle, and a low-frequency mass-transport feature including a flattened plateau (region ***D***) transitioning into a semicircular arc (region ***C***) [4,5]. As expected, the overall impedance is higher at 10% SOC, while ohmic and charge-transfer regions remain insensitive to flow rate at both SOCs, consistent with the literature. The low-frequency mass-transport region varies with flow rate at both SOCs. The explicit differentiation of regions ***D*** and ***C*** directly has not been systematically addressed in prior VFB EIS studies, with the exception of Zhang et al. who used a ferricyanide/ferrocyanide redox couple rather than vanadium [7]. This is consistent with DRT analyses showing multiple overlapping processes in the low-frequency region [9–11].

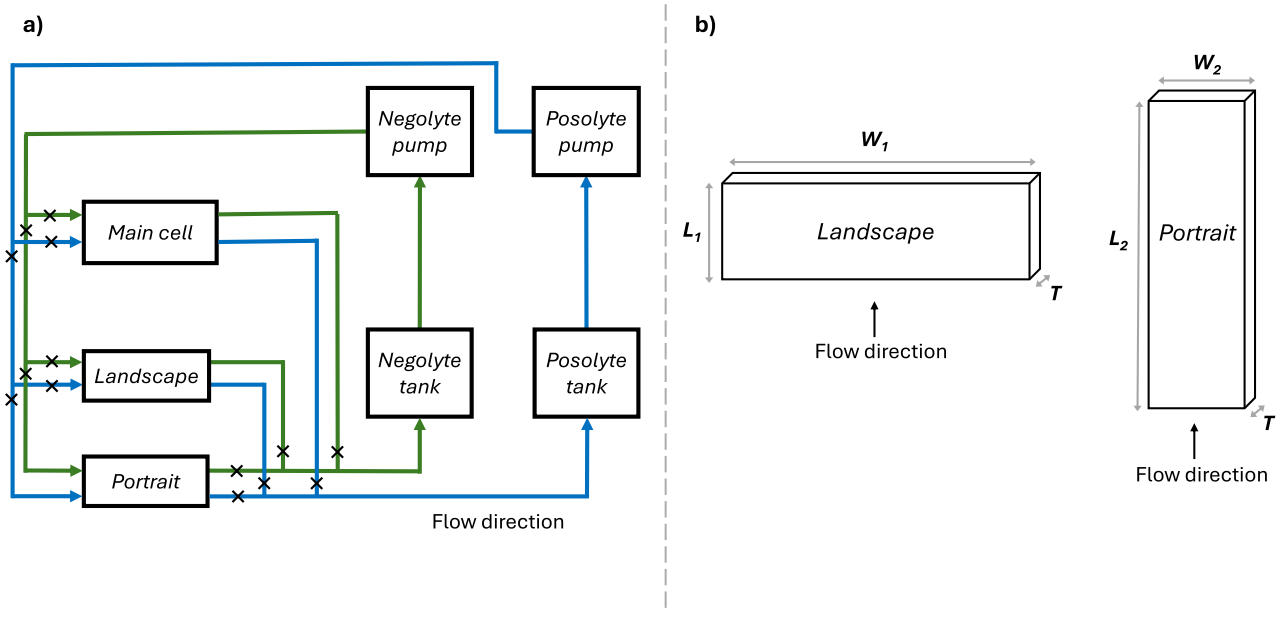

Fig. 1. Schematic illustration of (a) the experimental setup, where x represents the positions of the opening/closing clamps, and (b) the *landscape* and *portrait* felt electrode orientations relative to the flow direction.

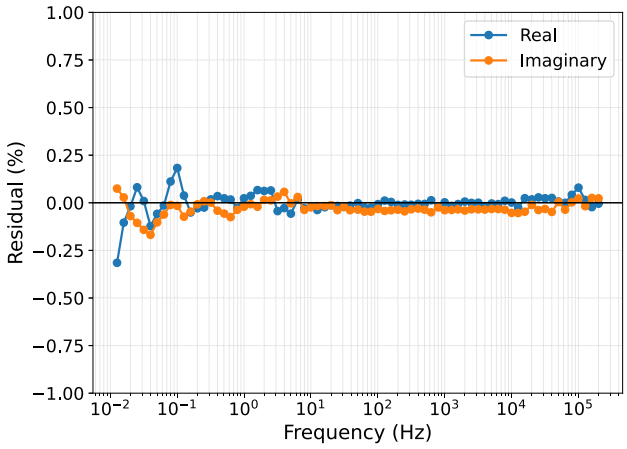

Fig. 2. Example residuals from the linear Kramers–Kronig consistency test for 10% SOC *landscape* cell at 5 ± 1 mL min^{-1}.

3.1. Assembly induced offsets

As *landscape* and *portrait* cell configuration were assembled as separate, manually tightened cells, small assembly induced variations are present in the higher-frequency response. These appear as an ohmic offset arising from differences in contact resistance, and as a change in the size of the first semicircle arising from slightly different felt compression between cells; the corresponding fitted values are reported in Table 3. Liu et al. showed that electrode compression predominantly affects the high- and mid- frequency response, with only a minor influence on the mass-transport resistance indicating that these assembly induced offsets do not affect the interpretation of regions ***D*** and ***C*** [12].

3.2. Decoupling volumetric flow rate and mean linear velocity

Since the cross-sectional area differs by a factor of four between the two configurations (Table 1), the mean linear velocity in the *portrait* cell is four times higher than in the *landscape* at the same volumetric flow rate, assuming uniform flow distribution through the felt (Table 2).

At 10% SOC, comparison of the two cells at the same volumetric flow rate of 5 ± 1 mL min^{-1} shows that the resistance of region ***D*** decreases by 0.008 Ω cm^2 as the mean linear velocity increases from 0.06 to 0.25 cm s^{-1}. By contrast, the resistance of region ***C*** changes comparatively little under these conditions. At approximately the same mean linear velocity of 0.25 cm s^{-1}, the resistance of region ***D*** remains comparable between the two configurations, whereas that of region ***C*** decreases by 0.23 Ω cm^2 as the volumetric flow rate increases from 5 ± 1 to 20 ± 1 mL min^{-1}. For 65% SOC the same trends are observed, however the resistances are less pronounced, showing that this effect is also seen at other SOC.

To further highlight the distinction of features ***D*** and ***C***, when flow rate and mean linear velocity are changed simultaneously for a given cell geometry (Fig. 3) both ***D*** and ***C*** shrink when increasing the flow rate from 5 ± 1 to 20 ± 1 mL min^{-1}. Overall, region ***C*** is considerably more sensitive to volumetric flow rate than region ***D*** is to mean linear velocity. This demonstrates that regions ***C*** and ***D*** respond differently to changes in volumetric flow rate and mean linear velocity and therefore do not reflect the same underlying physical process.

3.3. Physical interpretation of the two mass-transport contributions

Region ***D***, the higher frequency feature, is more sensitive to changes in mean linear velocity than to volumetric flow rate, consistent with a diffusion-dominated process near the carbon fibre surface, where increasing velocity reduces the Nernstian diffusion layer thickness and lowers the associated transport resistance [5].

As an approximation, treating individual fibres as single microelectrodes in stagnant electrolyte, the characteristic frequency of diffusion would scale with D_0/r^2, where D_0 is the diffusion coefficient and r is the characteristic length scale [17]. Using the diffusion coefficient of the V^{2+}/V^{3+} couple of 1.41×10^{-10} m^2 s^{-1} (as the negolyte is the limiting half-cell) and a fibre radius of 4×10^{-6} m, gives a characteristic frequency of approximately 10 Hz. This frequency is within the same order of magnitude as the characteristic point frequency of ***D*** in Table

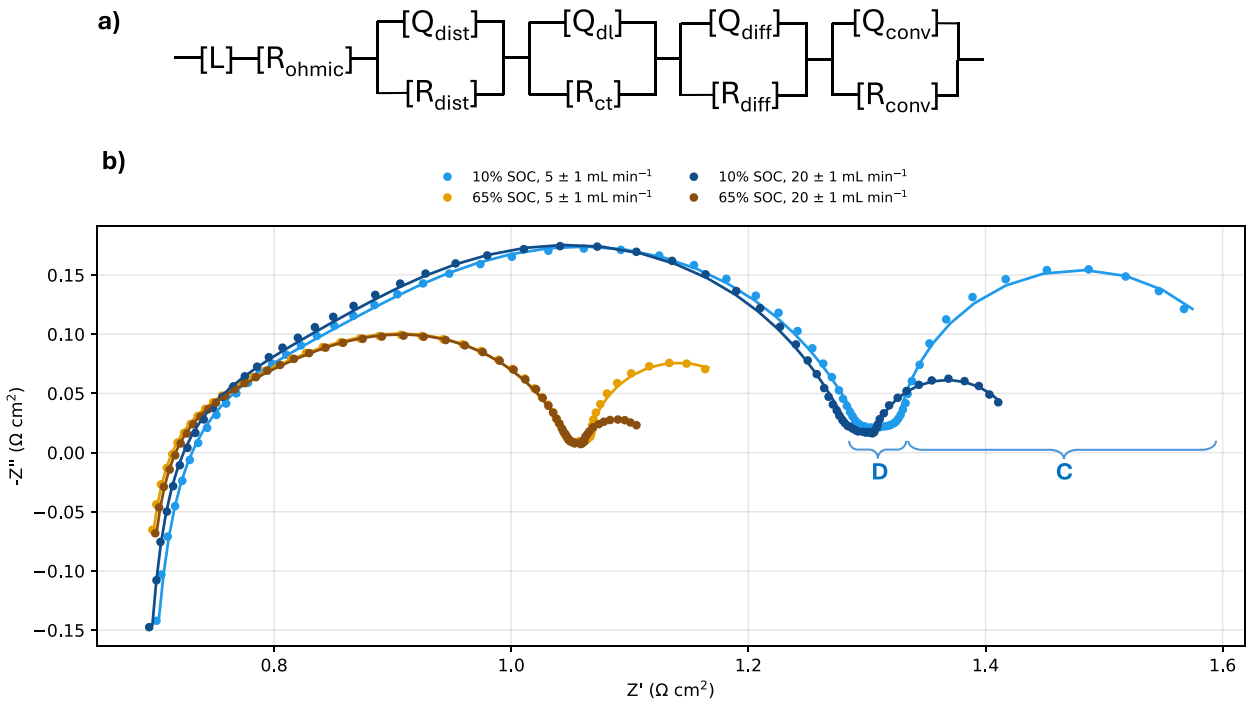

Fig. 3. (a) Empirical equivalent-circuit model fitted to the experimental data, where L represents the inductive response, R_{ohmic} the series ohmic resistance, $R_{dist}Q_{dist}$ the distributed ionic and electronic, $R_{ct}Q_{dl}$ the charge-transfer, $R_{diff}Q_{diff}$ the diffusion-dominated, and $R_{conv}Q_{conv}$ the convection-dominated contribution. (b) Nyquist plots of the EIS spectra for the *landscape* cell at 10% and 65% SOC, recorded at 5 ± 1 and 20 ± 1 mL min^{-1} with fitted empirical equivalent circuit model. The labels ***D*** and ***C*** indicate two low-frequency mass-transport features.

Table 2
Resistances and characteristic frequencies obtained from fitting the EIS spectra using the empirical equivalent-circuit model at 10% and 65% SOC for the *landscape* and *portrait* cell configurations at flow rates of 5 ± 1 and 20 ± 1 mL min^{-1}.

SOC	Cell	Q [mL min^{-1}]	u [cm s^{-1}]	***D*** resistance [Ω cm^2]	***D*** frequency [Hz]	***C*** resistance [Ω cm^2]	***C*** frequency [mHz]
10%	*Portrait*	5 ± 1	0.25 ± 0.05	0.015 ± 0.004	2.9 ± 0.5	0.35 ± 0.01	20.0 ± 0.4
	Landscape	5 ± 1	0.06 ± 0.01	0.023 ± 0.004	1.6 ± 0.2	0.31 ± 0.01	25.9 ± 0.3
	Landscape	20 ± 1	0.25 ± 0.02	0.014 ± 0.005	2.3 ± 0.5	0.12 ± 0.01	63.8 ± 1.6
65%	*Portrait*	5 ± 1	0.25 ± 0.05	0.009 ± 0.003	1.5 ± 0.3	0.16 ± 0.01	21.4 ± 0.4
	Landscape	5 ± 1	0.06 ± 0.01	0.013 ± 0.002	1.6 ± 0.2	0.15 ± 0.01	22.3 ± 0.4
	Landscape	20 ± 1	0.25 ± 0.02	0.008 ± 0.002	2.6 ± 0.4	0.06 ± 0.01	63.9 ± 1.6

2 [18,19]. However, the electrolyte is not stagnant and higher flow velocities would be expected to increase the characteristic frequency by thinning the diffusion layer. The discrepancy likely arises because the estimate neglects the complex transport within the porous felt. Its random fibre structure creates tortuous, non-uniform pathways, resulting in an effective diffusivity lower than the bulk molecular diffusivity. Pore-scale velocity variations also cause dispersion effects and non-uniform diffusion-layer thicknesses, which are not captured by the stagnant-electrolyte microelectrode approximation [20].

Region ***C***, which is more sensitive to volumetric flow rate, shows considerably stronger overall sensitivity to flow conditions, and is interpreted as a convection-dominated process at the electrode scale, driven by the total electrolyte supply and bulk electrolyte renewal rather than local fibre-scale hydrodynamics. Assuming plug flow through the cell and uniform charge-transfer current density through the electrode, the characteristic frequency of convection would be expected as $(2\pi\tau)^{-1}$, where τ is the residence time in the cell, estimated as the electrode open volume divided by the volumetric flow rate. The open volume is the product of geometric electrode volume and porosity. At the flow rates of 5 ± 1 and 20 ± 1 mL min^{-1}, this gives characteristic frequencies for convection-dominated process as 10 and 39 mHz, respectively. These are of the same order of magnitude as the measured characteristic frequencies of region ***C*** (Table 2). The remaining quantitative differences likely reflect the limitations of the simplified residence-time approximation as charge-transfer current density in porous electrodes is known to become spatially non-uniform due to potential gradients [21]. Such non-uniformity is expected to affect the effective transport time experienced by electroactive species, leading to deviations from the simple residence time prediction.

Although these frequency estimates involve significant simplifications and do not reproduce the experimental characteristic frequencies exactly (Table 2), they capture the correct order of magnitude and the key trends: region ***D*** appears at higher frequencies than region ***C***, and region ***C*** shifts strongly in magnitude and frequency with flow rate.

Consistent with this interpretation, the resistances associated with both features decrease as the relevant flow variable increases, reflecting faster electrolyte renewal. Moreover, the magnitude of both features were smaller at 65% than 10% SOC, but the characteristic frequencies did not change. In both cases this may be expected, because the frequencies are dependent on diffusion rates (feature ***D***) or flow rates (feature ***C***), but the magnitudes are dependent on the concentration of the electroactive species. It should be noted that these assignments are proposed on the basis of the observed flow variable dependence, and further quantitative analysis or modelling would be valuable to confirm them.

Zhang et al. similarly identified two separate contributions in the mass-transport region, with their higher-frequency plateau showing

Table 3
Empirical equivalent-circuit parameters extracted from the EIS measurements. Values are reported as the fitted value ± fitting uncertainty and are normalised by the electrode area. The weighted residual RMS represents the average relative mismatch between the measured and fitted complex impedance.

Cell orientation	10% SOC			65% SOC		
Flow rate [mL min^{-1}]	*Portrait* 5 ± 1	*Landscape* 5 ± 1	*Landscape* 20 ± 1	*Portrait* 5 ± 1	*Landscape* 5 ± 1	*Landscape* 20 ± 1
Ohmic and distributed contributions						
L [H cm^2]	$(9.36 \pm 0.15) \times 10^{-8}$	$(1.35 \pm 0.01) \times 10^{-7}$	$(1.36 \pm 0.01) \times 10^{-7}$	$(8.20 \pm 0.09) \times 10^{-8}$	$(6.91 \pm 0.07) \times 10^{-8}$	$(7.14 \pm 0.06) \times 10^{-8}$
R_{ohmic} [Ω cm^2]	0.59 ± 0.00	0.67 ± 0.00	0.67 ± 0.00	0.63 ± 0.00	0.68 ± 0.00	0.68 ± 0.00
R_{dist} [Ω cm^2]	0.20 ± 0.06	0.28 ± 0.04	0.27 ± 0.05	0.16 ± 0.04	0.17 ± 0.03	0.17 ± 0.02
Q_{dist} [S s$^{\alpha}$ cm^{-2}]	0.01 ± 0.01	0.01 ± 0.00	0.01 ± 0.01	0.02 ± 0.01	0.01 ± 0.00	0.01 ± 0.00
α_{dist}	0.57 ± 0.05	0.53 ± 0.03	0.53 ± 0.03	0.54 ± 0.03	0.55 ± 0.03	0.56 ± 0.03
f_{dist} [Hz]	5000 ± 2835	6382 ± 2037	5000 ± 1817	6651 ± 3220	11 409 ± 3437	11 632 ± 3010
Charge-transfer contribution						
R_{ct} [Ω cm^2]	0.31 ± 0.05	0.35 ± 0.03	0.35 ± 0.04	0.16 ± 0.04	0.21 ± 0.02	0.21 ± 0.02
Q_{dl} [S s$^{\alpha}$ cm^{-2}]	0.005 ± 0.0003	0.004 ± 0.0002	0.004 ± 0.0002	0.006 ± 0.0007	0.005 ± 0.0002	0.005 ± 0.0002
α_{dl}	0.83 ± 0.03	0.84 ± 0.02	0.85 ± 0.02	0.82 ± 0.04	0.81 ± 0.02	0.81 ± 0.02
f_{ct} [Hz]	420 ± 20	438 ± 10	413 ± 10	793 ± 39	823 ± 25	832 ± 22
Diffusion-dominated contribution						
R_{diff} [Ω cm^2]	0.015 ± 0.004	0.023 ± 0.004	0.014 ± 0.005	0.009 ± 0.003	0.013 ± 0.002	0.008 ± 0.002
Q_{diff} [S s$^{\alpha}$ cm^{-2}]	3.65 ± 1.19	4.37 ± 0.69	5.18 ± 1.62	11.76 ± 3.31	8.05 ± 1.08	8.69 ± 2.00
α_{diff}	1.00 ± 0.14	1.00 ± 0.09	1.00 ± 0.16	1.00 ± 0.17	1.00 ± 0.07	1.00 ± 0.11
f_{diff} [Hz]	2.87 ± 0.53	1.62 ± 0.17	2.28 ± 0.45	1.52 ± 0.30	1.61 ± 0.15	2.60 ± 0.37
Convection-dominated contribution						
R_{conv} [Ω cm^2]	0.35 ± 0.01	0.31 ± 0.01	0.12 ± 0.01	0.16 ± 0.01	0.15 ± 0.01	0.06 ± 0.01
Q_{conv} [S s$^{\alpha}$ cm^{-2}]	22.05 ± 0.54	20.04 ± 0.46	19.85 ± 1.03	47.57 ± 1.71	47.01 ± 1.16	42.02 ± 1.79
α_{conv}	1.00 ± 0.01	1.00 ± 0.01	0.98 ± 0.02	1.00 ± 0.01	1.00 ± 0.01	0.97 ± 0.02
f_{conv} [mHz]	20.46 ± 0.37	25.87 ± 0.31	63.79 ± 1.62	21.37 ± 0.44	22.34 ± 0.37	63.89 ± 1.60
Weighted residual RMS [%]	0.25	0.16	0.16	0.16	0.09	0.07

Q_{dist}, Q_{dl}, Q_{diff}, and Q_{conv} are the fitted constant-phase-element coefficients. Characteristic frequencies were calculated according to $f = (2\pi)^{-1}(RQ)^{-1/\alpha}$.

velocity dependence and their lower-frequency arc governed by hydrodynamic conditions at the fibre surface. However, their study varied only the volumetric flow rate while keeping the cell geometry fixed, meaning that the mean linear velocity changed simultaneously and its influence could not be separated from that of the flow rate [7]. While a direct one-to-one mapping between their mechanistic assignments and regions ***D*** and ***C*** is not straightforward, the present results are broadly consistent with the existence of two physically different processes with two distinctive characteristic frequencies.

4. Conclusions

EIS measurements were performed on two VFB cells containing carbon felt electrodes of identical geometric area but different flow orientations, resulting in a fourfold difference in cross-sectional area perpendicular to the flow direction. This allowed volumetric flow rate and mean linear electrolyte velocity to be varied independently - something not possible when flow rate alone is varied in a fixed cell geometry. Comparison of the two orientations revealed that the low-frequency mass-transport region contains two distinct contributions: region ***D***, the higher frequency feature, which is more sensitive to mean linear velocity and is interpreted as a diffusion-dominated process near the carbon fibre surface. Region ***C***, the lower frequency arc, is more sensitive to volumetric flow rate and corresponds to convection-dominated process associated with flow through the electrode. These assignments are based on how regions ***D*** and ***C*** respond differently to volumetric flow rate and mean linear flow velocity within the present experimental matrix. Establishing quantitative scaling relationships for both regions with their respective flow variables is beyond the scope of this short communication and is identified as a direction for future work.

These findings demonstrate that the low-frequency mass-transport feature should not be treated as a single finite-diffusion process or described by a simple shorted Warburg element, as this combines two contributions driven by different flow variables. This has direct implications for equivalent circuit and transmission line modelling of FBs, where separate treatment of these contributions may be necessary to accurately capture mass-transport losses under varying flow conditions. More broadly, the results show that the cell orientation influences the mass-transport response and therefore represents an important design parameter. Distinguishing these two transport processes also provides a framework for future studies investigating the effects of electrode microstructure such as pore size distribution and compression, on different mass-transport mechanisms.

CRediT authorship contribution statement

Zuzanna Borowiak: Writing – original draft, Visualization, Investigation, Formal analysis, Data curation, Conceptualization. **Jie Sun:** Writing – review & editing, Validation, Supervision, Resources, Funding acquisition, Conceptualization. **Adam H. Whitehead:** Writing – review & editing, Validation, Supervision, Methodology, Conceptualization. **Frank Rhein:** Writing – review & editing, Supervision.

Declaration of Generative AI and AI-assisted technologies in the writing process

During the preparation of this work the authors used ChatGPT (OpenAI) and Claude (Anthropic) in order to improve the readability and language of the manuscript. After using this tools, the authors reviewed and edited the content as needed and takes full responsibility for the content of the published article.

Declaration of competing interest

The authors declare that they have no known competing financial interests or personal relationships that could have appeared to influence the work reported in this paper.

Acknowledgements

This work is a part of PREDICTOR MSCA Doctoral Network funded by the European Union (Grant Agreement no. 101168943).

Data availability

Data will be made available on request.

References

[1] A. Adeniran, A. Bates, N. Schuppert, A. Menon, S. Park, Recent advances in aqueous redox flow battery research, J. Energy Storage 56 (2022) 106000, http://dx.doi.org/10.1016/j.est.2022.106000.

[2] J. Kim, H. Park, Recent advances in porous electrodes for vanadium redox flow batteries in grid-scale energy storage systems: A mass transfer perspective, J. Power Sources 545 (2022) 231904, http://dx.doi.org/10.1016/j.jpowsour.2022.231904.

[3] J. Huang, Y. Gao, J. Luo, S. Wang, C. Li, S. Chen, J. Zhang, Editors' choice—Review—Impedance response of porous electrodes: Theoretical framework, physical models and applications, J. Electrochem. Soc. 167 (16) (2020) 166503, http://dx.doi.org/10.1149/1945-7111/abc655.

[4] C.-N. Sun, F.M. Delnick, D.S. Aaron, A.B. Papandrew, M.M. Mench, T.A. Zawodzinski, Resolving losses at the negative electrode in all-vanadium redox flow batteries using electrochemical impedance spectroscopy, J. Electrochem. Soc. 161 (6) (2014) A981–A988, http://dx.doi.org/10.1149/2.045406jes.

[5] A.M. Pezeshki, R.L. Sacci, F.M. Delnick, D.S. Aaron, M.M. Mench, Elucidating effects of cell architecture, electrode material, and solution composition on overpotentials in redox flow batteries, Electrochim. Acta 229 (2017) 261–270, http://dx.doi.org/10.1016/j.electacta.2017.01.056.

[6] P. Sun, T. Suzuki, S. Tsushima, Investigation of kinetic and mass transport behaviors of V2+ and V3+ ions using symmetric vanadium redox flow battery configuration, J. Electrochem. Soc. 172 (2025) 050520, http://dx.doi.org/10.1149/1945-7111/add4a3.

[7] J. Zhang, Q. Gan, X. Yuan, Z. Xiang, Z. Fu, Z. Liang, Elucidating spatial distribution of electrochemical reaction in a porous electrode by electrochemical impedance spectra for flow batteries, Batteries 9 (1) (2023) 17, http://dx.doi.org/10.3390/batteries9010017.

[8] D. Qu, W. Ji, H. Qu, Probing process kinetics in batteries with electrochemical impedance spectroscopy, Commun. Mater. 3 (2022) 61, http://dx.doi.org/10.1038/s43246-022-00284-w.

[9] J. Schneider, T. Tichter, P. Khadke, R. Zeis, C. Roth, Deconvolution of electrochemical impedance data for the monitoring of electrode degradation in VRFB, Electrochim. Acta 336 (2020) 135510, http://dx.doi.org/10.1016/j.electacta.2019.135510.

[10] M. Schilling, M. Braig, K. Köble, R. Zeis, Investigating the V(IV)/V(V) electrode reaction in a vanadium redox flow battery – A distribution of relaxation times analysis, Electrochim. Acta 430 (2022) 141058, http://dx.doi.org/10.1016/j.electacta.2022.141058.

[11] M. Schilling, R. Zeis, Investigating the V(II)/V(III) electrode reaction in a vanadium redox flow battery – A distribution of relaxation times analysis, Electrochim. Acta 477 (2024) 143771, http://dx.doi.org/10.1016/j.electacta.2024.143771.

[12] B. Liu, S.B. Simonsen, J. Hjelm, Morphological properties and electrochemical performance for compressed carbon-fiber electrodes in redox flow batteries, J. Electrochem. Soc. 171 (4) (2024) 040503, http://dx.doi.org/10.1149/1945-7111/ad36e5.

[13] C.T.-C. Wan, R.R. Jacquemond, Y.-M. Chiang, K. Nijmeijer, F.R. Brushett, A. Forner-Cuenca, Non-solvent induced phase separation enables designer redox flow battery electrodes, Adv. Mater. 33 (16) (2021) 2006716, http://dx.doi.org/10.1002/adma.202006716.

[14] M.D. Murbach, B. Gerwe, N. Dawson-Elli, L.-k. Tsui, Impedance.py: A python package for electrochemical impedance analysis, J. Open Source Softw. 5 (52) (2020) 2349, http://dx.doi.org/10.21105/joss.02349.

[15] M. Schönleber, D. Klotz, E. Ivers-Tiffée, A method for improving the robustness of linear Kramers-Kronig validity tests, Electrochim. Acta 131 (2014) 20–27, http://dx.doi.org/10.1016/j.electacta.2014.01.034.

[16] J. Krakowiak, W. Bącalski, G. Lentka, P. Peljo, P. Ślepski, Three modes of electrochemical impedance spectroscopy measurements performed on vanadium redox flow battery, Sustain. Mater. Technol. 40 (2024) e00957, http://dx.doi.org/10.1016/j.susmat.2024.e00957.

[17] A. Lasia, Electrochemical Impedance Spectroscopy and its Applications, Springer, New York, 2014, http://dx.doi.org/10.1007/978-1-4614-8933-7.

[18] E. Sum, M. Skyllas-Kazacos, A study of the V(II)/V(III) redox couple for redox flow cell applications, J. Power Sources 15 (2) (1985) 179–190, http://dx.doi.org/10.1016/0378-7753(85)80071-9.

[19] C.-N. Sun, F.M. Delnick, D.S. Aaron, A.B. Papandrew, M.M. Mench, T.A. Zawodzinski, Probing electrode losses in all-vanadium redox flow batteries with impedance spectroscopy, ECS Electrochem. Lett. 2 (5) (2013) A43, http://dx.doi.org/10.1149/2.001305eel.

[20] Q. Ma, L. Xing, H. Su, W. Zhang, W. Yang, Q. Xu, Numerical investigation on the dispersion effect in vanadium redox flow battery, Chem. Eng. J. 393 (2020) 124753, http://dx.doi.org/10.1016/j.cej.2020.124753.

[21] M. Becker, N. Bredemeyer, N. Tenhumberg, T. Turek, Kinetic studies at carbon felt electrodes for vanadium redox-flow batteries under controlled transfer current density conditions, Electrochim. Acta 252 (2017) 12–24, http://dx.doi.org/10.1016/j.electacta.2017.07.062.